

Tensor cross interpolation approach for quantum impurity problems based on the weak-coupling expansion

Shuta Matsuura,¹ Hiroshi Shinaoka,² Philipp Werner,³ and Naoto Tsuji^{1,4}

¹*Department of Physics, University of Tokyo, Hongo, Tokyo 113-0033, Japan*

²*Department of Physics, Saitama University, Saitama 338-8570, Japan*

³*Department of Physics, University of Fribourg, 1700 Fribourg, Switzerland*

⁴*RIKEN Center for Emergent Matter Science (CEMS), Wako, Saitama 351-0198, Japan*

(Dated: January 23, 2025)

We apply the tensor cross interpolation (TCI) algorithm to solve equilibrium quantum impurity problems with high precision based on the weak-coupling expansion. The TCI algorithm, a kind of active learning method, factorizes high-dimensional integrals that appear in the perturbative expansion into a product of low-dimensional ones, enabling us to evaluate higher-order terms efficiently. This method is free from the sign problem which quantum Monte Carlo methods sometimes suffer from, and allows one to directly calculate the free energy. We benchmark the TCI impurity solver on an exactly solvable impurity model, and find good agreement with the exact solutions. We also incorporate the TCI impurity solver into the dynamical mean-field theory to solve the Hubbard model, and show that the metal-to-Mott insulator transition is correctly described with comparable accuracy to the Monte Carlo methods. Behind the effectiveness of the TCI approach for quantum impurity problems lies the fact that the integrands in the weak-coupling expansion naturally have a low-rank structure in the tensor-train representation.

I. INTRODUCTION

Solving quantum impurity problems is a fundamental issue in condensed matter physics. They describe localized impurity states hybridized with a bath of noninteracting particles, providing a basis for the understanding of the Kondo effect [1], a prototypical phenomenon in quantum many-body physics. The impurity model setup is realized not only in solid states [2–4] but also in artificial quantum systems such as quantum dots [5–7] and ultracold atoms [8–10]. Quantum impurity problems also play a central role in the dynamical mean-field theory (DMFT) [11–14] (or more generally, in quantum embedding methods [15]), which is a powerful tool to study strongly correlated systems in high dimensions. It has been applied to study the metal-to-Mott insulator transition [16–19], high-temperature superconductors [20–23] and disordered systems [24–26].

Various methods have been developed to solve quantum impurity problems, among which the continuous-time quantum Monte Carlo (CT-QMC) method [27–31] is widely used as a versatile and numerically exact impurity solver. In CT-QMC, one expands the partition function and observables into infinite series, which can be classified into weak- and strong-coupling ones depending on the expansion parameter. Each term in the expansion (corresponding to a Feynman diagram) consists of high-dimensional integrals, which can be evaluated by stochastic sampling. While statistical errors can be controlled within the framework, there are several drawbacks: The errors scale as $1/\sqrt{N}$ (N is the number of samples), so that the convergence is relatively slow (in the recently proposed quasi-Monte Carlo method the scaling is improved to $1/N$ [32, 33]). One may also encounter the infamous sign problem when the method is applied to multi-orbital models, multi-site clusters, spin-orbit cou-

pled systems, and nonequilibrium impurity problems. It is also not straightforward to calculate the free energy using the CT-QMC solver.

Some of these issues may be overcome by the recently developed tensor cross interpolation (TCI) algorithm [34–39], in which multi-variable integrands to be integrated in a perturbative expansion are regarded as high-dimensional tensors. The TCI approximates such a high-dimensional tensor by a one-dimensional network of tensors called a tensor train or a matrix product state (MPS), which can be constructed from partial (selected) information of the original tensor through a certain “interpolation” scheme. This is to be contrasted to the singular value decomposition for constructing MPSs, which uses the full information of the tensor and becomes computationally demanding if the dimension of the tensor is large. The TCI is particularly useful when the high-dimensional tensor has a low-rank structure, for which an efficient (but often heuristic) search algorithm allows to find a quasi-optimal tensor-train representation.

Once the low-rank tensor-train representation of the integrand is obtained, one can evaluate high-dimensional integrals efficiently by separately performing a series of one-dimensional integrations. Even if the integrand shows an oscillatory behavior with positive and negative contributions, the integration can be evaluated accurately with the TCI (as long as it has a low-rank structure), so that the calculation does not practically suffer from the sign problem. Furthermore, one can directly calculate the partition function and the free energy with the TCI approach. Previously, TCI has been used for equilibrium impurity problems based on the strong-coupling expansion [40]. There are also applications to nonequilibrium impurity problems using the weak-coupling expansion with a simple hybridization function [38] and the self-consistent strong-coupling expansion [41, 42].

In this paper, we apply the TCI algorithm to equilibrium impurity problems formulated within the weak-coupling framework, which has not yet been explored. The weak-coupling approach has an advantage in studying cluster problems, for which the strong-coupling expansion is less suited due to the exponentially large dimension of the local Hilbert space. We first apply the TCI solver to an exactly solvable impurity model. The results show that the integrand in the weak-coupling expansion indeed has a low-rank structure, which allows us to calculate the expansion up to the 40th order. We find good agreement between the TCI and exact solutions. We also employ the TCI as an impurity solver for DMFT to solve the Hubbard model on the Bethe lattice, and compare the results with those of CT-QMC. While the method is based on the weak-coupling expansion, we find that the metal-to-Mott insulator crossover is well reproduced with a comparable accuracy to CT-QMC. The weak-coupling TCI solver can also be used to explore the first-order Mott transition slightly below the critical temperature where the metallic and insulating solutions coexist. We furthermore show results for the free energy of the lattice system, which is not easy to evaluate by CT-QMC.

The paper is organized as follows. Section II provides an outline of the formalism. We review the weak-coupling expansion of the impurity problem, and explain how the TCI algorithm can be used to evaluate high-dimensional integrals. Section III presents the results of the weak-coupling TCI impurity solver. In Sec. III A, we apply the TCI solver to the exactly solvable impurity model, and show that the TCI algorithm can efficiently evaluate high-order contributions. In Sec. III B, we solve the Hubbard model in the Mott transition (crossover) regime by incorporating the TCI solver with DMFT. The results given by the TCI solver agree with those of the quantum Monte Carlo method with high precision. Section IV discusses the implication of the results and future perspectives of the weak-coupling TCI impurity solver.

II. METHOD

A. Weak-coupling expansion of the impurity problem

In this section, we review the weak-coupling expansion for the single-site impurity problem using the path-integral formalism. The effective action of the single-site

impurity model is given by

$$S = S_0 + S_{\text{int}}, \quad (1a)$$

$$S_0 = \int_0^\beta d\tau \sum_\sigma c_\sigma^*(\tau) \partial_\tau c_\sigma(\tau) + \int_0^\beta d\tau d\tau' \sum_\sigma c_\sigma^*(\tau) \Delta_\sigma(\tau - \tau') c_\sigma(\tau'), \quad (1b)$$

$$S_{\text{int}} = \int_0^\beta d\tau U \left(c_\uparrow^*(\tau) c_\uparrow(\tau) - \frac{1}{2} \right) \left(c_\downarrow^*(\tau) c_\downarrow(\tau) - \frac{1}{2} \right), \quad (1c)$$

where $c_\sigma^*(\tau)$ is the creation operator of an electron with spin σ at imaginary time τ , β is the inverse temperature, $\Delta_\sigma(\tau)$ denotes the hybridization function, which represents the coupling between the impurity and bath degrees of freedom, and U is the interaction parameter. The chemical potential is set to $\mu = U/2$ to ensure that the system is half filled. The extension to systems away from half filling is straightforward, but will not be discussed in this paper. Using this action, the partition function and the impurity Green's function can be expressed in the path-integral form as

$$Z = \int \mathcal{D}c^* \mathcal{D}c e^{-S}, \quad (2)$$

$$G_\sigma(\tau) = -\frac{1}{Z} \int \mathcal{D}c^* \mathcal{D}c c_\sigma(\tau) c_\sigma^*(0) e^{-S}, \quad (3)$$

respectively.

By expanding Eqs. (2) and (3) with respect to U and applying Wick's theorem, we obtain formulae for the weak-coupling expansion [27, 31]:

$$\frac{Z}{Z_0} = \sum_{n=0}^{\infty} (-U)^n \int_{S_n^{0,\beta}} d\tau_1 \cdots d\tau_n (\det \mathbf{D}_n^\uparrow) (\det \mathbf{D}_n^\downarrow), \quad (4)$$

$$G_\sigma(\tau) = \frac{Z_0}{Z} \sum_{n=0}^{\infty} (-U)^n \int_{S_n^{0,\beta}} d\tau_1 \cdots d\tau_n \times (\det \tilde{\mathbf{D}}_n^\sigma) (\det \mathbf{D}_n^{\bar{\sigma}}), \quad (5)$$

where \mathbf{D}_n^σ and $\tilde{\mathbf{D}}_n^\sigma$ are $n \times n$ and $(n+1) \times (n+1)$ matrices defined by

$$\mathbf{D}_n^\sigma = \begin{pmatrix} \mathcal{G}_\sigma(0^-) - 1/2 & \cdots & \mathcal{G}_\sigma(\tau_1 - \tau_n) \\ \vdots & \ddots & \vdots \\ \mathcal{G}_\sigma(\tau_n - \tau_1) & \cdots & \mathcal{G}_\sigma(0^-) - 1/2 \end{pmatrix}, \quad (6)$$

$$\tilde{\mathbf{D}}_n^\sigma = \begin{pmatrix} \mathcal{G}_\sigma(\tau) & \mathcal{G}_\sigma(\tau - \tau_1) & \cdots & \mathcal{G}_\sigma(\tau - \tau_n) \\ \mathcal{G}_\sigma(\tau_1) & \mathcal{G}_\sigma(0^-) - 1/2 & \cdots & \mathcal{G}_\sigma(\tau_1 - \tau_n) \\ \vdots & \vdots & \ddots & \vdots \\ \mathcal{G}_\sigma(\tau_n) & \mathcal{G}_\sigma(\tau_n - \tau_1) & \cdots & \mathcal{G}_\sigma(0^-) - 1/2 \end{pmatrix}, \quad (7)$$

$$\mathcal{G}_\sigma(\tau) = -(\partial_\tau + \Delta_\sigma(\tau))^{-1}, \quad (8)$$

$\mathcal{G}_\sigma(\tau)$ is the Weiss field, Z_0 is the partition function for the impurity model described by the noninteracting action S_0 , and $S_n^{0,\beta}$ denotes a simplex defined by

$$S_n^{a,b} = \{(\tau_1, \dots, \tau_n) \in \mathbb{R}^n \mid a \leq \tau_1 \leq \dots \leq \tau_n \leq b\}. \quad (9)$$

The index $\bar{\sigma}$ represents the spin polarization opposite to σ .

By truncating the infinite series (4) and (5) at a finite order n_{\max} , we obtain the following approximate expressions for the partition function and the Green's function:

$$\frac{Z}{Z_0} \simeq \sum_{n=0}^{n_{\max}} (-U)^n \int_{S_n^{0,\beta}} d\tau_1 \cdots d\tau_n (\det \mathbf{D}_n^\uparrow) (\det \mathbf{D}_n^\downarrow), \quad (10)$$

$$G_\sigma(\tau) \simeq \frac{Z_0}{Z} \sum_{n=0}^{n_{\max}} (-U)^n \int_{S_n^{0,\beta}} d\tau_1 \cdots d\tau_n \times (\det \tilde{\mathbf{D}}_n^\sigma) (\det \mathbf{D}_n^{\bar{\sigma}}). \quad (11)$$

B. Dynamical mean-field theory

Impurity problems play an important role in the dynamical mean-field theory (DMFT), which maps the lattice model to an effective impurity model. In this mapping, the hybridization function is self-consistently determined under the assumption that the lattice self-energy be local in space [12]. Solving the impurity problem is a key step in DMFT, enabling us to compute the local Green's function of the strongly correlated lattice system in high spatial dimensions. This section briefly reviews the formulation of DMFT for a simple case.

Let us consider the Hubbard model on the Bethe lattice with connectivity z at half filling ($\mu = U/2$). Its Hamiltonian is given by

$$H = -\frac{t}{\sqrt{z}} \sum_{\langle i,j \rangle, \sigma} (c_{i\sigma}^\dagger c_{j\sigma} + \text{H.c.}) + \sum_i U \left(n_{i\uparrow} - \frac{1}{2} \right) \left(n_{i\downarrow} - \frac{1}{2} \right), \quad (12)$$

where t is the nearest-neighbor hopping amplitude. The local Green's function for the lattice system with the Hamiltonian (12) is defined by

$$G_{\text{loc}}(\tau) = -\left\langle T_\tau c_{i\sigma}(\tau) c_{i\sigma}^\dagger(0) \right\rangle, \quad (13)$$

where T_τ is the time-ordering operator. The local lattice Green's function is identical to that of the single-site impurity model [Eq. (1)] with

$$\Delta_\sigma(\tau) = t^2 G_{\text{loc}}(\tau), \quad (14)$$

when we consider the infinite coordination limit $z \rightarrow \infty$ [12, 43] (with bandwidth $4t$). Here, we assume that the

system is in the paramagnetic phase, where the local Green's function does not depend on spin.

Note that $G_{\text{loc}}(\tau)$ to be computed is included in the definition of the impurity problem [Eq. (5)]. $G_{\text{loc}}(\tau)$ must be determined self-consistently by iterating the following loop until convergence is reached: Starting from an initial guess of the Weiss field $\mathcal{G}(\tau)$, (i) compute $G(\tau)$ by Eqs. (10) and (11), (ii) obtain $\Delta_\sigma(\tau)$ from Eq. (14) by setting $G_{\text{loc}}(\tau) = G(\tau)$, (iii) solve Eq. (8) to update $\mathcal{G}(\tau)$.

C. TCI algorithm

In this section, we review the tensor cross interpolation (TCI) and how it can be used to evaluate high-dimensional integrals based on Ref. [39]. The TCI approximates a tensor by a product of its low-dimensional slices, which is called a tensor train. Here, we mainly focus on the definition of the TCI approximation and its key properties. We briefly describe the algorithm used to construct the tensor train, for the details of which we refer to the paper of Y. Núñez-Fernández *et al.* [39].

1. Matrix cross interpolation

We first introduce the matrix cross interpolation (CI) [34–39], which forms a basis of the TCI approximation. Let us consider an $M \times N$ matrix A . We define the set of the row and column indices of A as $\mathbb{I} = \{1, 2, \dots, M\}$ and $\mathbb{J} = \{1, 2, \dots, N\}$, respectively, and write the subset of \mathbb{I} , \mathbb{J} with size χ ($\leq \text{rank } A$) as $I = \{i_1, i_2, \dots, i_\chi\} \subset \mathbb{I}$ and $J = \{j_1, j_2, \dots, j_\chi\} \subset \mathbb{J}$. The $\chi \times \chi$ submatrix (or slices) of A which consists of rows and columns with indices in I , J is denoted by $A(I, J)$, i.e.,

$$[A(I, J)]_{\alpha\beta} = A_{i_\alpha j_\beta}. \quad (15)$$

In a similar manner, an $M \times \chi$ submatrix $A(\mathbb{I}, J)$ and a $\chi \times N$ submatrix $A(I, \mathbb{J})$ are defined. With these notations, the CI formula approximates the matrix A by a rank- χ matrix \tilde{A} defined as

$$A \simeq A(\mathbb{I}, J) A(I, J)^{-1} A(I, \mathbb{J}) =: \tilde{A}. \quad (16)$$

The matrix $A(I, J)$ is called a pivot matrix, and its elements are called pivots. Note that the data size is compressed from $\mathcal{O}(MN)$ to $\mathcal{O}(\max\{M, N\}\chi)$ by the CI formula when A is approximated with a small number of pivots ($\chi \ll M, N$).

The matrix \tilde{A} has two important properties that ensure the validity of the approximation in Eq. (16). The first one is

$$A(\mathbb{I}, J) = \tilde{A}(\mathbb{I}, J), \quad A(I, \mathbb{J}) = \tilde{A}(I, \mathbb{J}), \quad (17)$$

which means that the approximation reproduces the original matrix A in the selected rows I and columns J , and hence all the other elements, not included in I or J , are

interpolated. The second one is that if χ is equal to the rank of the matrix A , the approximation becomes exact, i.e., $A = \tilde{A}$.

To achieve a high-quality approximation, I and J should be chosen carefully. Although finding the optimal pivots is computationally demanding, a heuristic search algorithm based on the partial rank-revealing LU (prrLU) decomposition is known to find suboptimal ones [39]. By repeating the process of searching for the matrix element with largest modulus and performing the Gauss elimination χ times, one can construct the rank- χ CI approximation of a given matrix.

2. Tensor cross interpolation

The tensor cross interpolation (TCI) is an extension of the matrix CI that approximates a tensor by a product of its low-dimensional slices [34–39]. Let us consider a tensor A with n legs labeled by $\sigma_1, \sigma_2, \dots, \sigma_n$. We assume that the index σ_ℓ ($1 \leq \ell \leq n$) takes values from the set $\mathbb{S}_\ell = \{1, 2, \dots, d_\ell\}$, which means that A is a $d_1 \times d_2 \times \dots \times d_n$ tensor. Let us define the set of the row multi-indices \mathbb{I}_ℓ and column multi-indices \mathbb{J}_ℓ for $1 \leq \ell \leq n$ by

$$\mathbb{I}_\ell = \mathbb{S}_1 \times \mathbb{S}_2 \times \dots \times \mathbb{S}_\ell, \quad (18)$$

$$\mathbb{J}_\ell = \mathbb{S}_\ell \times \mathbb{S}_{\ell+1} \times \dots \times \mathbb{S}_n, \quad (19)$$

and their subsets by $I_\ell \subset \mathbb{I}_\ell$ and $J_\ell \subset \mathbb{J}_\ell$. For convenience, we define I_0 and J_{n+1} as a set which consists of an empty tuple,

$$I_0 = J_{n+1} = \{()\}. \quad (20)$$

We require the number of the elements of the subset I_ℓ and $J_{\ell+1}$ to be equal to each other for $1 \leq \ell \leq n-1$,

$$|I_\ell| = |J_{\ell+1}| =: \chi_\ell \quad (1 \leq \ell \leq n-1). \quad (21)$$

For $\ell = 0$ and n , we define $\chi_0 = |I_0| = 1$ and $\chi_n = |J_{n+1}| = 1$. The slices of the tensor A are defined in a similar manner to the matrix case, e.g., $A(I_\ell, J_{\ell+1})$ is a $\chi_\ell \times \chi_\ell$ matrix, and $A(I_{\ell-1}, \mathbb{S}_\ell, J_{\ell+1})$ is a $\chi_{\ell-1} \times d_\ell \times \chi_\ell$ three-leg tensor. Using these notations, the TCI approximation \tilde{A} of A is defined as

$$\begin{aligned} A_{\sigma_1 \dots \sigma_n} &\simeq T_1^{\sigma_1} P_1^{-1} T_2^{\sigma_2} P_2^{-1} \dots P_{n-1}^{-1} T_n^{\sigma_n} \\ &=: \tilde{A}_{\sigma_1 \dots \sigma_n}. \end{aligned} \quad (22)$$

Here, P_ℓ is a $\chi_\ell \times \chi_\ell$ matrix defined by

$$P_\ell = A(I_\ell, J_{\ell+1}), \quad (23)$$

T_ℓ is a $\chi_{\ell-1} \times d_\ell \times \chi_\ell$ three-leg tensor defined by

$$T_\ell = A(I_{\ell-1}, \mathbb{S}_\ell, J_{\ell+1}), \quad (24)$$

and $T_\ell^{\sigma_\ell}$ is a $\chi_{\ell-1} \times \chi_\ell$ matrix whose elements are related to those of T_ℓ by

$$[T_\ell^{\sigma_\ell}]_{ij} = [T_\ell]_{i\sigma_\ell j}. \quad (25)$$

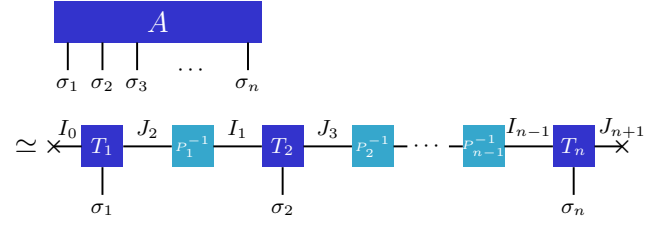


FIG. 1. Tensor-train decomposition of a tensor $A_{\sigma_1 \dots \sigma_n}$ in the TCI. P_ℓ and T_ℓ represent zero-dimensional and one-dimensional slices of the tensor A defined by Eqs. (23) and (24), respectively. By decomposing $A_{\sigma_1 \dots \sigma_n}$ into a product of small tensors, one can perform high-dimensional integrals efficiently.

The matrix P_ℓ is called a pivot matrix, and $\chi = \max_\ell \chi_\ell$ is the maximum bond dimension or the rank of the tensor train. This decomposition is diagrammatically represented in Fig. 1.

The TCI approximation has a property similar to Eq. (17). To state this property, we introduce the nesting condition. If $I_\ell \subset I_{\ell-1} \times \mathbb{S}_\ell$, I_ℓ is said to be nested with respect to $I_{\ell-1}$, and we write $I_{\ell-1} < I_\ell$. In the same way, if $J_\ell \subset \mathbb{S}_\ell \times J_{\ell+1}$, J_ℓ is said to be nested with respect to $J_{\ell+1}$, and we write $J_\ell > J_{\ell+1}$. When $I_0 < I_1 < \dots < I_{\ell-1}$ and $J_{\ell+1} > J_{\ell+2} > \dots > J_n$ holds, \tilde{A} satisfies

$$A(I_{\ell-1}, \mathbb{S}_\ell, J_{\ell+1}) = \tilde{A}(I_{\ell-1}, \mathbb{S}_\ell, J_{\ell+1}). \quad (26)$$

This means that the TCI approximation can reproduce some of the elements of the original tensor, and the other elements are interpolated if the nesting condition is satisfied.

As is the case in the matrix CI, the quality of the TCI approximation heavily depends on the choice of I_ℓ and J_ℓ . To find the suboptimal I_ℓ and J_ℓ , the two-site TCI algorithm [39] is available. In this algorithm, the matrix CI with prrLU is repeatedly applied to the two-dimensional slices of the tensor A to construct a tensor train. If a tensor A has a structure that can be approximated with a low-rank tensor train, it is empirically known that this algorithm can almost always construct such a low-rank tensor train. One of the notable features of this algorithm is that it does not require the full information of the tensor A to construct the tensor-train representation. This is in contrast to the singular value decomposition, which requires the full information of the tensor and is less efficient for decomposing a high-dimensional tensor. Since the TCI algorithm actively samples a few important elements during the construction of the tensor train, it can be regarded as a kind of active learning algorithm.

3. Evaluating high-dimensional integrals by TCI

To evaluate the Green's function of the impurity model, we have to perform the high-dimensional inte-

grals appearing in Eqs. (10) and (11). In this work, we evaluate these integrals by combining Gauss–Kronrod (GK) quadrature and the tensor-train decomposition generated by the TCI algorithm following the approach in Ref. [38, 39]. This section reviews how the high-dimensional integrals can be performed with the GK quadrature and the TCI algorithm.

Let us consider an n -dimensional integral of a continuous function $f(x_1, \dots, x_n)$ over a hypercube,

$$\mathcal{I} = \int_{[0,1]^n} d^n \mathbf{x} f(\mathbf{x}). \quad (27)$$

By using the GK quadrature rule, the integral can be approximated as a discrete sum,

$$\begin{aligned} \mathcal{I} &\simeq \sum_{\sigma_1=1}^d \cdots \sum_{\sigma_n=1}^d w_{\sigma_1} \cdots w_{\sigma_n} f(x_{\sigma_1}, \dots, x_{\sigma_n}) \\ &=: \sum_{\sigma_1=1}^d \cdots \sum_{\sigma_n=1}^d A_{\sigma_1 \dots \sigma_n}, \end{aligned} \quad (28)$$

where x_i are the zeros of the Legendre polynomials and Stieltjes polynomials, w_i are the corresponding weights, and d denotes the order of the GK quadrature which is set to $d = 15$ in this work. The computational cost of this n -fold sum is $\mathcal{O}(d^n)$, which grows exponentially with respect to the integral dimension n . Note that the weights w_{σ_ℓ} are absorbed in the definition of the tensor A (although it is also possible to formulate the method without absorbing them).

To reduce the computational cost, we use the TCI algorithm [34, 37, 39]. In the TCI approach, the tensor $A_{i_1 \dots i_n}$ is decomposed into a product of small tensors,

$$\begin{aligned} A_{\sigma_1 \dots \sigma_n} &\simeq T_1^{\sigma_1} P_1^{-1} T_2^{\sigma_2} P_2^{-1} \cdots P_{n-1}^{-1} T_n^{\sigma_n} \\ &= M_1^{\sigma_1} M_2^{\sigma_2} \cdots M_n^{\sigma_n} \end{aligned} \quad (29)$$

by sampling few elements of $A_{i_1 \dots i_n}$, where P_ℓ and $T_\ell^{\sigma_\ell}$ are defined by Eqs. (23)–(25) and $M_\ell^{\sigma_\ell}$ is defined by

$$M_\ell^{\sigma_\ell} = \begin{cases} T_\ell^{\sigma_\ell} P_\ell^{-1} & \text{if } 1 \leq \ell \leq n-1, \\ T_n^{\sigma_n} & \text{if } \ell = n. \end{cases} \quad (30)$$

By this decomposition, the original n -fold summation can be reduced to n independent summations,

$$\mathcal{I} \simeq \left(\sum_{\sigma_1=1}^d M_1^{\sigma_1} \right) \left(\sum_{\sigma_2=1}^d M_2^{\sigma_2} \right) \cdots \left(\sum_{\sigma_n=1}^d M_n^{\sigma_n} \right). \quad (31)$$

The resulting computational cost is $\mathcal{O}(nd\chi^2) \ll \mathcal{O}(d^n)$, where χ is the maximum bond dimension of the tensor-train decomposition.

To implement the TCI algorithm, we utilize `TensorCrossInterpolation.jl` introduced in Ref. [39]. It provides the TCI algorithm based on the prLU decomposition, and allows one to construct the tensor-train representation without inverting the pivot matrix P_ℓ , which

can be ill-conditioned. Also, a global search algorithm to find pivots is available, which helps to avoid being stuck in a subpart of the whole space while sampling the elements of the tensor. These features have not been incorporated in the previous works [38, 40]. While the algorithm described above does not preserve the nesting condition by default, practically no problem has been observed in the numerical calculations [39].

D. Computation of the partition function

In this section, we discuss the technical aspects of performing the integrals that appear in the expression of the partition function [Eq. (10)]. The technique explained in this section and the following section is based on the paper of A. Erpenbeck *et al.* [40]. The map employed in this section is described in detail in Appendix A.

In order to perform high-dimensional integrals based on the method described in Sec. II C, the integral domain must be a hypercube. Since the integral in Eq. (10),

$$\mathcal{I}_n = (-U)^n \int_{S_n^{0,\beta}} d\tau_1 \cdots d\tau_n P(\tau_1, \dots, \tau_n), \quad (32)$$

where $P(\tau_1, \dots, \tau_n) = (\det \mathbf{D}_n^\uparrow)(\det \mathbf{D}_n^\downarrow)$, is defined on the simplex $S_n^{0,\beta}$, one has to change the integral variables to rewrite the integral over a simplex in the form of an integral over a hypercube $[0,1]^n$. To this end, we use a bijective map, $h_{0,\beta} : [0,1]^n \rightarrow S_n^{0,\beta}$, which is defined in Eqs. (A1), (A5) and (A9). By relating $(v_1, \dots, v_n) \in [0,1]^n$ with $(\tau_1, \dots, \tau_n) \in S_n^{0,\beta}$ through

$$(\tau_1, \dots, \tau_n) = h_n^{0,\beta}(v_1, \dots, v_n), \quad (33)$$

the integral \mathcal{I}_n can be expressed as

$$\begin{aligned} \mathcal{I}_n &= (-U)^n \int_{[0,1]^n} dv_1 \cdots dv_n P(h_n^{0,\beta}(v_1, \dots, v_n)) \\ &\quad \times J_{h_n^{0,\beta}}(v_1, \dots, v_n), \end{aligned} \quad (34)$$

where $J_{h_n^{0,\beta}}(v_1, \dots, v_n)$ is the Jacobian for the transformation (33) explicitly given by Eq. (A10). Let us remark here that this Jacobian is separable, i.e., can be factorized as

$$J_{h_n^{0,\beta}}(v_1, \dots, v_n) = A_1(v_1) \cdots A_n(v_n), \quad (35)$$

which means that it has a low-rank structure.

For later convenience, we define the function

$$\tilde{P}(v_1, \dots, v_n) = P(h_n^{0,\beta}(v_1, \dots, v_n)) J_{h_n^{0,\beta}}(v_1, \dots, v_n), \quad (36)$$

and write \mathcal{I}_n as

$$\mathcal{I}_n = (-U)^n \int_{[0,1]^n} dv_1 \cdots dv_n \tilde{P}(v_1, \dots, v_n). \quad (37)$$

We may then express the partition function as

$$\frac{Z}{Z_0} \simeq \sum_{n=1}^{n_{\max}} (-U)^n \int_{[0,1]^n} dv_1 \cdots dv_n \tilde{P}(v_1, \dots, v_n). \quad (38)$$

E. Computation of the Green's function

In this section, we discuss how to apply the TCI algorithm to the integral in Eq. (11),

$$\mathcal{J}_n^\sigma(\tau) = (-U)^n \int_{S_n^{0,\beta}} d\tau_1 \cdots d\tau_n Q^\sigma(\tau_1, \cdots, \tau_n; \tau), \quad (39)$$

where $Q^\sigma(\tau_1, \cdots, \tau_n; \tau) = (\det \tilde{D}_n^\sigma)(\det D_n^\sigma)$. Similarly to the case of the partition function, we have to change the integral variables so that the integral domain becomes a hypercube. However, the situation is more complicated due to the existence of a non-integrated variable (τ) and the discontinuity of the integrand. We will explain how to deal with these issues in the following subsections.

1. Treatment of the non-integrated variable τ

Unlike the integral appearing in the partition function [Eq. (32)], the one in the Green's function [Eq. (39)] involves the variable τ , which is not integrated.

There are (at least) two ways to deal with it. The first one is to get the tensor-train approximation of $Q^\sigma(\tau_1, \cdots, \tau_n; \tau)$ at each sampling point τ , and calculate $\mathcal{J}_n^\sigma(\tau)$. Although this method is stable, the computational cost is proportional to the number of sampling points τ , which scales as $\mathcal{O}(\log \omega_{\max} \beta)$ when using the intermediate representation basis [44, 45] (ω_{\max} is an ultraviolet cutoff on the real-frequency axis).

Another method is to treat τ as a leg of the tensor, obtain a tensor-train representation for this enlarged tensor, and then take a summation over the legs other than τ . In this method, we can get the Green's function for all the sampling points τ with a one-shot TCI. Since the tensor becomes larger by adding a new leg, the low-rank structure of the tensor might be lost. However, in the case studied here, the low-rank structure is retained, as in the case of the strong-coupling expansion [40]. Thus, we adopt the second method below.

We generate the sampling points τ by using `SparseIR.jl` [44–47] in the DMFT analysis presented later. It is known that the Matsubara Green's functions are highly compressible and the whole information of the Green's function can be reconstructed from a few sampling points based on the intermediate representation [44]. The library provides us with a routine to generate the sampling points and reconstruct the Green's function. This technique is useful to reduce the computational cost for the calculation of the Green's function in the TCI algorithm.

2. Change of variables

As in the case of the partition function, the integral in Eq. (39) is defined over a simplex, which needs to be transformed into a hypercube. Furthermore, since \tilde{D}_n^σ

depends on $\mathcal{G}_\sigma(\tau - \tau_i)$ that has a discontinuous jump at $\tau = \tau_i$, the integrand $Q^\sigma(\tau_1, \cdots, \tau_n; \tau)$ is also discontinuous at $\tau_i = \tau$ for $1 \leq i \leq n$.

To eliminate the discontinuities, we divide the simplex $S_n^{0,\beta}$ into smaller $n + 1$ regions ($S_k^{0,\tau} \times S_{n-k}^{\tau,\beta}$ with $k = 0, 1, \dots, n$),

$$\begin{aligned} \mathcal{J}_n^\sigma(\tau) &= (-U)^n \sum_{k=0}^n \int_{S_k^{0,\tau}} d\tau_1 \cdots d\tau_k \\ &\times \int_{S_{n-k}^{\tau,\beta}} d\tau_{k+1} \cdots d\tau_n Q^\sigma(\tau_1, \cdots, \tau_n; \tau). \end{aligned} \quad (40)$$

In the region labeled by k , τ satisfies $\tau_1 \leq \cdots \leq \tau_k \leq \tau \leq \tau_{k+1} \leq \cdots \leq \tau_n$, and thus, the integrand $Q^\sigma(\tau_1, \cdots, \tau_n; \tau)$ is continuous within each domain.

To deform the integral domain to a hypercube, we perform the following variable transformation for each k :

$$(\tau_1, \cdots, \tau_k) = h_k^{0,\tau}(v_1, \cdots, v_k), \quad (41)$$

$$(\tau_{k+1}, \cdots, \tau_n) = h_{n-k}^{\tau,\beta}(v_{k+1}, \cdots, v_n). \quad (42)$$

With these transformations, the integration domain changes from $S_k^{0,\tau} \times S_{n-k}^{\tau,\beta}$ to $[0, 1]^k \times [0, 1]^{n-k} = [0, 1]^n$, and we get

$$\begin{aligned} \mathcal{J}_n^\sigma(\tau) &= \sum_{k=0}^n (-U)^n \int_{[0,1]^n} dv_1 \cdots dv_n Q_k^\sigma(v_1, \cdots, v_n; \tau) \\ &\times J_{h_k^{0,\tau}}(v_1, \cdots, v_k) J_{h_{n-k}^{\tau,\beta}}(v_{k+1}, \cdots, v_n). \end{aligned} \quad (43)$$

Here, $Q_k^\sigma(v_1, \cdots, v_n; \tau)$ is the function that satisfies

$$Q_k^\sigma(v_1, \cdots, v_n; \tau) = Q^\sigma(\tau_1, \cdots, \tau_n; \tau), \quad (44)$$

where (τ_1, \cdots, τ_n) and (v_1, \cdots, v_n) are related through Eqs. (41) and (42). As in the case of the partition function, the Jacobian is separable, i.e., it can be written in the form of

$$\begin{aligned} J_{h_k^{0,\tau}}(v_1, \cdots, v_k) J_{h_{n-k}^{\tau,\beta}}(v_{k+1}, \cdots, v_n) \\ = B(\tau) B_1(v_1) \cdots B_n(v_n). \end{aligned} \quad (45)$$

For later convenience, we define a function,

$$\begin{aligned} \tilde{Q}_k^\sigma(v_1, \cdots, v_n; \tau) &= Q_k^\sigma(v_1, \cdots, v_n; \tau) \\ &\times J_{h_k^{0,\tau}}(v_1, \cdots, v_k) J_{h_{n-k}^{\tau,\beta}}(v_{k+1}, \cdots, v_n), \end{aligned} \quad (46)$$

and write $\mathcal{J}_n^\sigma(\tau)$ as

$$\mathcal{J}_n^\sigma(\tau) = \sum_{k=0}^n (-U)^n \int_{[0,1]^n} dv_1 \cdots dv_n \tilde{Q}_k^\sigma(v_1, \cdots, v_n; \tau). \quad (47)$$

With this, the Green's function can be expressed as

$$\begin{aligned} G_\sigma(\tau) &\simeq \frac{Z_0}{Z} \sum_{n=1}^{n_{\max}} \sum_{k=0}^n (-U)^n \int_{[0,1]^n} dv_1 \cdots dv_n \\ &\times \tilde{Q}_k^\sigma(v_1, \cdots, v_n; \tau). \end{aligned} \quad (48)$$

3. Discrete summation over k

In addition to the integral over v_1, \dots, v_n , there appears a discrete summation over k in Eq. (48). We have tried three ways to perform the discrete sum with respect to k .

The first method is to get the tensor-train approximation of $\sum_{k=0}^n \tilde{Q}_k^\sigma(v_1, \dots, v_n; \tau)$ by applying the TCI algorithm and integrate it over a hypercube by summing over the indices of the tensor train. We found that this method works up to the order of $n_{\max} \sim 20$, but it produces non-smooth Green's functions for higher orders.

The second method treats k as an additional leg of the tensor, together with $\tau_1, \dots, \tau_n, \tau$, and applies the TCI algorithm to this extended tensor. By summing over the indices corresponding to τ_1, \dots, τ_n and k in the obtained tensor train, we can perform the integral and discrete summation in Eq. (48) at once. Since the computational cost of evaluating $\tilde{Q}_k^\sigma(v_1, \dots, v_k; \tau)$ is approximately $n+1$ times smaller than that of $\sum_{k=0}^n \tilde{Q}_k^\sigma(v_1, \dots, v_n; \tau)$, the TCI algorithm runs faster in this implementation as compared to the first one. However, the bond dimension required to achieve an accurate tensor-train approximation can grow higher due to the additional leg corresponding to k . In fact, we observed that the Green's function calculated up to the 30th order by this methods was not smooth even with a maximum bond dimension $\chi = 400$.

The third method is to find the tensor-train representation of $\tilde{Q}_k^\sigma(v_1, \dots, v_n)$ by the TCI algorithm and calculate $\int_{[0,1]^n} dv_1 \dots dv_n \tilde{Q}_k^\sigma(v_1, \dots, v_n)$ for each k independently, and finally take a summation over k . This method is more stable than the other methods since the integrand has a simpler structure. With this approach, we can obtain a smooth Green's function even if the bond dimension is taken to be $\chi = 50$. Therefore, we adopt the third method in the analysis presented in Sec. III.

F. Rough estimate of the required maximum order

Whenever we calculate the partition function or the Green's function for the impurity problem, we have to choose the maximum order n_{\max} in such a way that the truncation does not change the results much. Here, we roughly estimate n_{\max} required to obtain an accurate result.

Let us focus on the DMFT effective impurity problem for the Hubbard model in the Mott regime. In this parameter region, the local Green's function and hence the hybridization function quickly decays in imaginary time. Therefore, we can neglect $\Delta_\sigma(\tau)$ in Eq. (8), and $\mathcal{G}_\sigma(\tau)$ is approximately given by a constant,

$$\mathcal{G}_\sigma(\tau) \approx -1/2 \quad \text{for } 0 \leq \tau \leq \beta. \quad (49)$$

Although this approximation might be oversimplified, it captures the typical behavior of the Weiss field in the low-temperature and strong-coupling region. Within this

approximation, the partition function can be analytically evaluated as

$$\frac{Z}{Z_0} = \sum_{n:\text{even}} \frac{1}{n!} \left(\frac{\beta U}{4} \right)^n. \quad (50)$$

This means that the even-order contribution is proportional to the Poisson distribution with both the mean and the variance being equal to $\beta U/4$. When $\beta U/4 \gg 1$, the Poisson distribution can be further approximated by the Gaussian distribution. From the property of the Gaussian distribution, we can see that if we take

$$n_{\max} \simeq \frac{\beta U}{4} + 3\sqrt{\frac{\beta U}{4}}, \quad (51)$$

it can cover 3σ of the Gaussian distribution, which is sufficient to get an almost exact value of Z/Z_0 .

So far, we have focused on the low-temperature and strong-coupling regime. As we increase the temperature or decrease the interaction strength, $|\mathcal{G}_\sigma(\tau)|$ generally decreases from $1/2$, and this will shift the center of the distribution to a smaller value than $\beta U/4$. Therefore, the estimate (51) is also sufficient for the weak-coupling and high-temperature regime.

III. RESULTS

A. Exactly solvable impurity model

We first benchmark our calculations with an exactly solvable impurity model, which corresponds to an impurity problem for the Falicov–Kimball model in DMFT [48]. The action is given by Eq. (1) with $\Delta_\downarrow(\tau) = 0$, which means that the spin-down impurity electron does not hybridize with the bath degrees of freedom. In this case, we can easily integrate out the spin-down electrons for arbitrary $\Delta_\uparrow(\tau)$. The Green's function of the spin-up electron can be calculated analytically as

$$G_\uparrow(i\omega_n) = \frac{1}{2} \left(\frac{1}{\mathcal{G}_\uparrow(i\omega_n)^{-1} - U/2} + \frac{1}{\mathcal{G}_\uparrow(i\omega_n)^{-1} + U/2} \right), \quad (52)$$

where

$$\mathcal{G}_\uparrow(i\omega_n) = \frac{1}{i\omega_n - \Delta_\uparrow(i\omega_n)}. \quad (53)$$

One of the simplest choices for $\Delta_\uparrow(\tau)$ is $\Delta_\uparrow(\tau) = 0$. In this case, $\mathcal{G}_\uparrow(\tau) = \mathcal{G}_\downarrow(\tau) = -1/2$ for $0 \leq \tau \leq \beta$, and $P(h_n^{0,\beta}(v_1, \dots, v_n))$ in Eq. (36) and $Q_k^\sigma(v_1, \dots, v_n)$ in Eq. (46) become constant. As mentioned in Sec. IID and Sec. IIE, the Jacobians are separable, so that the entire integrands for the partition function and the Green's function are also separable in this case. Therefore, they trivially have tensor-train representations with rank $\chi = 1$, which is not suitable for the benchmark.

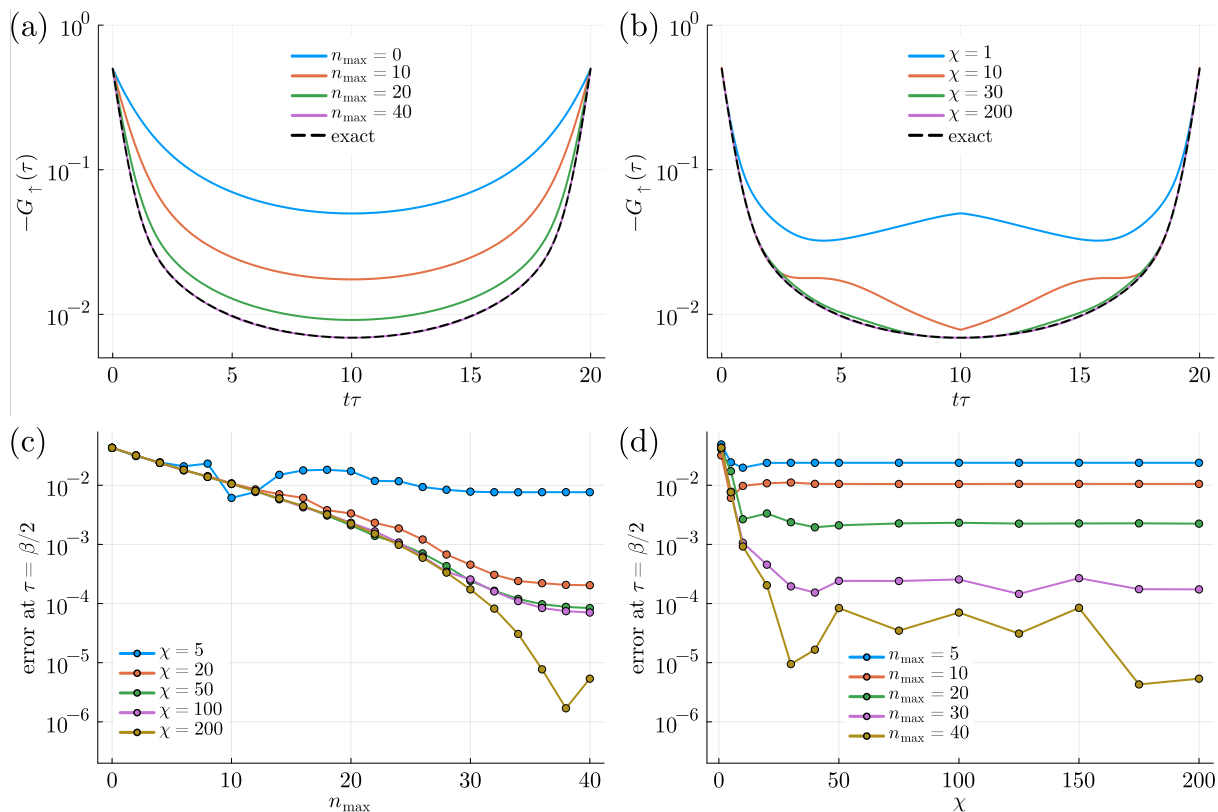


FIG. 2. Results of the weak-coupling TCI solver for the exactly solvable impurity model with $\mathcal{G}_\downarrow(\tau) = -1/2$ and $\mathcal{G}_\uparrow(\tau)$ given by Eq. (54). The parameters are set to $\beta = 20/t$, $U = 5t$. [(a), (b)] The Green's functions obtained from the TCI solver and the exact solution for (a) several maximum orders n_{\max} with the maximum bond dimension $\chi = 200$, and (b) several χ with $n_{\max} = 40$. [(c), (d)] The difference of the Green's functions at $\tau = \beta/2$ between the TCI and the exact solution plotted as a function of (c) n_{\max} and (d) χ .

To benchmark the performance of the weak-coupling TCI impurity solver, we take $\mathcal{G}_\uparrow(\tau)$ to be the noninteracting Green's function on the Bethe lattice with infinite coordination number,

$$\mathcal{G}_\uparrow(\tau) = - \int_{-2t}^{2t} d\omega \frac{\sqrt{4t^2 - \omega^2}}{2\pi t^2} \frac{e^{-\tau\omega}}{1 + e^{-\beta\omega}}, \quad (54)$$

which is a typical initial Green's function used in DMFT calculations.

In Fig. 2(a) and (b), we show the numerical results for the Green's function $G_\uparrow(\tau)$ with $\beta = 20/t$ and $U = 5t$ calculated by the weak-coupling TCI impurity solver, which are compared with the exact solution. Figure 2(a) shows how the result changes by increasing the maximum order n_{\max} while keeping the maximum bond dimension fixed at $\chi = 200$. With $n_{\max} = 20$, there is a difference of around 10^{-3} as compared to the exact one, while the result with $n_{\max} = 40$ agrees with the exact solution almost perfectly. This is consistent with the rough estimate we discussed in Sec II F. In Fig. 2(b), the Green's function for several values of χ are plotted with n_{\max} being fixed at $n_{\max} = 40$. One can see that the tensor-train approximation of rank $\chi = 30$ gives a smooth result which almost agrees with the exact solution.

This fact indicates that the integrand in the weak-coupling expansion has a low-rank structure that can be searched by the TCI algorithm. Since the Jacobians are separable as mentioned in Sec. IID and Sec. IIE, whether the whole integrand has a low-rank structure or not depends on the structure of $P(h_n^{0,\beta}(v_1, \dots, v_n))$ and $Q_k^\sigma(v_1, \dots, v_n)$ in Eqs. (36) and (46). In the low-temperature regime, $\mathcal{G}_\uparrow(\tau)$ exhibits a plateau over a wide range of $0 < \tau < \beta$. As a result, $P(h_n^{0,\beta}(v_1, \dots, v_n))$ and $Q_k^\sigma(v_1, \dots, v_n)$ take almost constant values in most parts of the hypercube. Thus we can expect that the integrands are almost separable in the low temperature regime. This may be the reason why the TCI algorithm works well in the weak-coupling expansion. The effective impurity model appearing in DMFT also shares a similar property. In the zero-temperature or strong-coupling limit, the local Green's function $G_{\text{loc}}(\tau)$ approaches zero in almost the entire interval $0 < \tau < \beta$, and the Weiss field $\mathcal{G}_\sigma(\tau)$, which is related to $G_{\text{loc}}(\tau)$ through Eqs. (8) and (14), becomes almost constant over $0 < \tau < \beta$. Thus, the integrand is almost separable in these limits, and it is expected to be so also in the finite but low-temperature and strong-coupling regimes.

In Fig. 2(c) and (d), we present a more detailed analy-

sis of the convergence of the results with respect to n_{\max} and χ . In Fig. 2(c), we plot the deviation of the Green's function from the exact solution at $\tau = \beta/2$ as a function of n_{\max} . Different curves correspond to different fixed values of χ . For $\chi \leq 100$, we can see a saturation behavior, i.e., the results are not improved anymore even if n_{\max} is increased. Although evaluating the integral with n_{\max} close to or larger than 40 is computationally demanding with $\chi \leq 100$, the error becomes smaller than 10^{-4} , which is often enough for practical purposes. For $\chi = 200$, we do not find an obvious sign of saturation up to $n_{\max} = 40$, where the precision of 10^{-5} can be reached.

Figure 2(d) shows the deviation of the Green's function at $\tau = \beta/2$ as a function of χ with several values of n_{\max} . For $n_{\max} \leq 30$, the error decreases exponentially with respect to the bond dimension in the range of $0 \leq \chi \leq 15$. For $\chi > 50$, the error remains nearly constant. This indicates that the integral with $n_{\max} \leq 30$ can be efficiently computed by the weak-coupling TCI. For $n_{\max} = 40$, the error does not exhibit a plateau over the range of $0 \leq \chi \leq 200$, but setting $\chi = 200$ results in an error of 10^{-5} , which is sufficiently small.

The computational cost of the algorithm can be estimated as follows. To obtain the n th-order contribution to the Green's function, we have to decompose $n + 1$ different tensors with $n + 1$ legs by TCI. Here, the $n + 1$ different tensors correspond to the integrands for each k in Eq. (48). When decomposing one of them with a bond dimension χ , we have to sample its elements $\mathcal{O}(\chi^2 dn)$ times [39], where d is the dimension of the legs corresponding to the order of the GK quadrature in this work. Since the sampling of elements requires a calculation of a determinant of an $n \times n$ matrix, whose computational cost scales as $\mathcal{O}(n^3)$, the total cost for sampling becomes $\mathcal{O}(\chi^2 dn^4)$. Therefore, recalling the computation of the n th-order term requires the decomposition of $n + 1$ tensors, the computational cost for evaluating the n th-order term is $\mathcal{O}(\chi^2 dn^5)$. To obtain the contribution from the first order to the n_{\max} th order, the overall computational cost amounts to $\mathcal{O}(\chi^2 dn_{\max}^6)$. Combining this scaling with the rough estimate (51), the cost can be expressed in terms of β and U as $\mathcal{O}(\chi^2 d(\beta U)^6)$.

B. Dynamical mean-field theory applications

Here we apply the weak-coupling TCI impurity solver to DMFT to study the Hubbard model on the Bethe lattice with infinite coordination number [Eq. (12)]. We will show results for two inverse temperatures, $\beta = 16/t$ and $\beta = 20/t$. The critical endpoint of the Mott transition is known to lie in between these two temperatures [19] (see Fig. 3). Thus, we expect to observe a metal-insulator crossover at $\beta = 16/t$ and a Mott transition at $\beta = 20/t$.

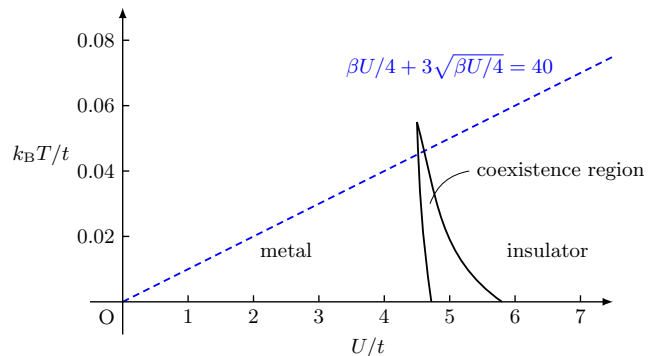


FIG. 3. DMFT phase diagram for the Hubbard model on the Bethe lattice. The dashed line ($\beta U/4 + 3\sqrt{\beta U/4} = 40$) corresponds to a rough estimate of the boundary above which the weak-coupling TCI solver in the current setup can provide accurate results for the maximum order $n_{\max} \simeq 40$ and bond dimension $\chi \lesssim 200$.

1. Analysis of the crossover region

Figure 4(a)-(c) shows the results of the weak-coupling TCI solver for $\beta = 16/t$, which is slightly above the Mott transition endpoint. From the analysis of the exactly solvable model, we concluded that a bond dimension $\chi \simeq 50$ provides reasonably accurate results. Therefore, we first iterate the DMFT loop with $\chi = 50$ to achieve an approximate convergence. Subsequently, we increase the bond dimension to $\chi = 200$ to obtain final results with high precision. The maximum order n_{\max} is determined from the rough estimate (51).

In Fig. 4(a), we plot the local Green's functions calculated by the weak-coupling TCI solver, and the continuous-time quantum Monte Carlo methods based on the hybridization expansion (CT-HYB) [28] and the auxiliary field (CT-AUX) [30] formulation. As we increase the interaction strength U , $-G_{\text{loc}}(\beta/2)$, which is roughly proportional to the density of states at the Fermi level, approaches zero. This behavior reflects the metal-insulator crossover. In the parameter range shown in Fig. 4(a), the results of the TCI solver agree well with those of the QMC methods. The difference is on the order of 10^{-4} or even smaller, suggesting that the crossover region can be studied by the TCI solver with an accuracy comparable to that of the QMC methods. There are slight differences between CT-HYB and CT-AUX, which give an idea of the uncertainties associated with the Monte Carlo errors and possibly a lack of full convergence of the DMFT loop. The two Monte Carlo methods are based on different types of perturbative expansions (CT-HYB is based on the strong-coupling expansion, while CT-AUX is based on the weak-coupling expansion). In the crossover regime, CT-HYB is more efficient than CT-AUX [29].

In the TCI approach, we can evaluate the doublon number $d = \langle n_{i\uparrow} n_{i\downarrow} \rangle$, which captures the effect of strong

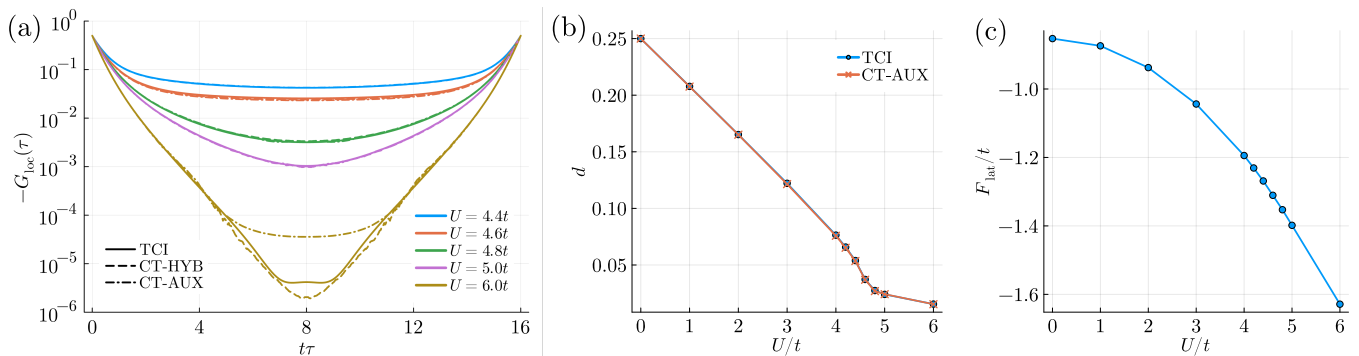


FIG. 4. DMFT results for the half-filled Hubbard model on the Bethe lattice at $\beta = 16/t$. (a) Local Green's functions for several values of U in the metal-insulator crossover region. The solid, dashed and dash-dotted lines correspond to the results of the weak-coupling TCI, CT-HYB, and CT-AUX impurity solvers, respectively. In the TCI calculations, the maximum bond dimension is set to $\chi = 200$ in the last few DMFT loops. The maximum order n_{max} is determined by the rough estimate (51). (b) Doublon number $d = \langle n_{i\uparrow}n_{i\downarrow} \rangle$ as a function of U calculated by the weak-coupling TCI and CT-AUX impurity solvers. (c) Free energy of the lattice model, F_{lat} , as a function of U calculated by the weak-coupling TCI solver.

correlations, by using the formula [31],

$$d = \frac{1}{4} - \frac{\langle n \rangle_{\text{wc}}}{\beta U}, \quad (55)$$

where $\langle n \rangle_{\text{wc}}$ is the average order of the weak-coupling expansion of the partition function defined by

$$\langle n \rangle_{\text{wc}} = \frac{Z_0}{Z} \sum_{n=0}^{\infty} n \mathcal{I}_n. \quad (56)$$

Since the TCI solver evaluates \mathcal{I}_n for each n , the doublon number can be readily extracted. The doublon numbers calculated by the weak-coupling TCI solver and the CT-AUX solver are shown in Fig. 4(b). The results are consistent with each other. The curve exhibits a different slope for interaction strengths below and above $U \simeq 4.7t$, which corresponds to the metal-insulator crossover.

The free energy, which is difficult to access by the CT-QMC solver, can be directly calculated by the TCI solver. The free energy of the effective impurity model is related to Z/Z_0 by

$$F_{\text{imp}} = -\frac{1}{\beta} \ln \left(\frac{Z}{Z_0} \right) - \frac{2}{\beta} \ln \left(2 \prod_{n=-\infty}^{\infty} \left(1 - \frac{\Delta(i\omega_n)}{i\omega_n} \right) \right), \quad (57)$$

where the second term corresponds to the free energy of the noninteracting impurity model [48]. The free energy of the whole lattice model, F_{lat} , is related to F_{imp} by [49, 50]

$$F_{\text{lat}} = F_{\text{imp}} - \frac{1}{\beta} \sum_{n=-\infty}^{\infty} \frac{\Delta(i\omega_n)^2}{t^2}. \quad (58)$$

The free energy F_{lat} calculated by Eqs. (57) and (58) is shown in Fig. 4(c). We can see that F_{lat} monotonically decreases with U . Since there is no Mott transition at $\beta = 16/t$, the free energy is a smooth function of U .

2. Analysis of the Mott transition

Next we show the results around the Mott transition in the Hubbard model on the Bethe lattice at $\beta = 20/t$. As the temperature is lowered, the required perturbation order n_{max} increases, making the calculation more challenging. Our weak-coupling TCI solver can explore the temperature regime slightly below the critical endpoint of the Mott transition (Fig. 3).

Figure 5(a) shows the local Green's functions calculated by the TCI solver. One can observe that the value of the Green's function at $\tau = \beta/2$ suddenly drops when one slightly changes the interaction strength from $U = 4.68t$ to $U = 4.72t$. This discontinuous jump of $-G_{\text{loc}}(\beta/2)$ is an indication of the first-order Mott transition.

As shown in Fig. 5(b), at $U = 4.7t$, the Green's function converges to two different solutions depending on the initial condition. Starting from the Green's function at $U = 4.68t$, it converges to the metallic solution depicted by the blue line in Fig. 5(b), while starting from the Green's function at $U = 4.72t$, it converges to the insulating solution depicted by the orange line. This coexistence of two solutions is a typical feature of a first-order phase transition. Even though we use the weak-coupling expansion, the coexistence behavior in the strong-coupling regime can be well captured by the TCI solver.

The doublon number $d = \langle n_{i\uparrow}n_{i\downarrow} \rangle$ around the Mott transition is shown in Fig. 5(c). Since our TCI solver provides two stable solutions of the DMFT loop for $4.68t < U < 4.71t$, the doublon number exhibits a hysteresis loop in this region.

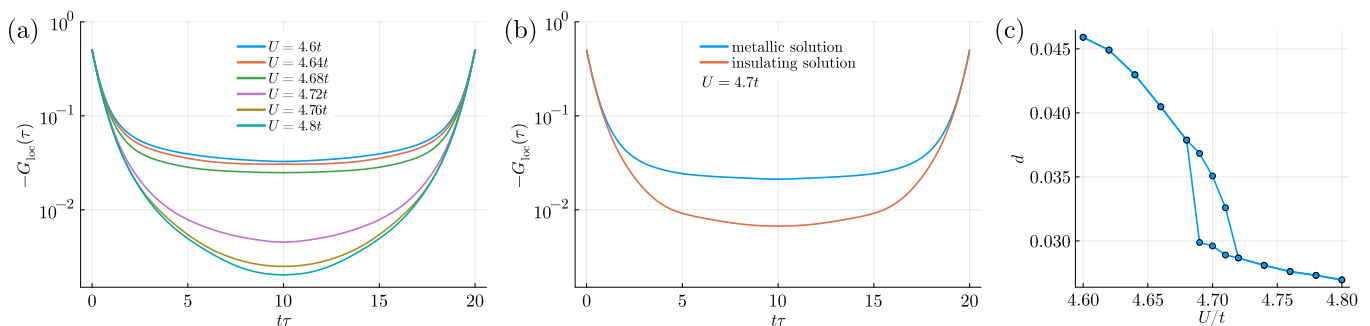


FIG. 5. DMFT results obtained by the weak-coupling TCI impurity solver for the half-filled Hubbard model on the Bethe lattice at $\beta = 20/t$. (a) Local Green's function for several representative values of U . The value of the Green's function at $\tau = \beta/2$ suddenly drops at $U \simeq 4.7t$, which is an indication of the Mott transition. (b) The two coexisting DMFT solutions for $U = 4.7t$. The blue line (metallic solution) is obtained by starting the DMFT loop with the solution for $U = 4.68t$, while the orange line (insulating solution) is obtained by starting with the solution for $U = 4.72t$. (c) Doublon number $d = \langle n_{i\uparrow}n_{i\downarrow} \rangle$ as a function of U . There is a hysteresis loop in the region $4.69t \lesssim U \lesssim 4.71t$.

3. Current limitations of the weak-coupling TCI solver

To finish this section, let us discuss the limitations of the current weak-coupling TCI solver. From the analysis of the exactly solvable model and the comparison with CT-QMC in the DMFT calculations, we found that the weak-coupling TCI solver works well when the maximum order is $n_{\max} \lesssim 40$. However, for the low-temperature and strong-coupling region where $n_{\max} > 40$ is required, obtaining accurate results is difficult for our TCI solver, even with $\chi = 200$. This is because the integrals on the right hand side of Eq. (48) can be either positive or negative depending on k . In the Mott regime, the low-temperature Green's function takes very small negative values in a wide τ interval, and this is a consequence of the cancellation between positive and negative contributions in the summation over k . To evaluate the small negative values of the Green's function accurately, we need to calculate both positive and negative contributions of high-order terms with high precision, and this requires a larger bond dimension χ and more computational time (this should be distinguished from the sign problem of QMC methods, since the issue may depend on the quantity to be calculated).

In practice, we observed that the Green's function calculated by the TCI solver can become slightly positive when $\beta = 30/t, U = 5t$ even though we set the bond dimension to $\chi = 200$, and this positive part survives even after several DMFT loops. This result violates the inequality $G_{\text{loc}}(\tau) < 0$ ($0 < \tau < \beta$), which should be satisfied by the physical Green's functions.

In Fig. 3, we show a rough estimate of the boundary (51) ($\beta U/4 + 3\sqrt{\beta U/4} = 40$) at which the maximum order that we have to consider reaches $n_{\max} = 40$. Above this line, our TCI solver works stably with bond dimension $\chi \lesssim 200$, and the simulations can be run with small-scale parallelization. If one can handle larger bond dimensions, the boundary can be pushed down.

In this work, we use the TCI algorithm which tries to minimize the error of each element of the tensor. The alternative choice is to use the one that minimizes the environment error, i.e., the error of the summation of all the elements [38, 39]. This may improve the accuracy of the TCI solver, since we are interested in integrated values and not each individual element. Also, there could be an alternative variable transformation that may mitigate the positive and negative cancellation problem of the Green's functions. We will leave these issues as a future work.

IV. DISCUSSIONS

We presented a weak-coupling tensor cross interpolation (TCI) solver for equilibrium quantum impurity problems. A major challenge in the weak-coupling expansion lies in evaluating high-order integrals, whose computational cost grows exponentially with their dimensions. By employing the TCI algorithm, the integrand is decomposed into a product of matrix-valued functions, enabling an efficient evaluation of high-dimensional integrals through one-dimensional ones, which scales polynomially with respect to the dimension. With a suitable variable transformation, the integrand becomes a continuous function over a hypercube with a low-rank structure, enabling an efficient calculation.

We have benchmarked the performance of our TCI solver for two setups: an exactly solvable impurity model and the DMFT solution of the Hubbard model with maximum perturbation order up to $n_{\max} = 40$. For the exactly solvable model, we find that the error of the Green's function at $\tau = \beta/2$ decays exponentially as a function of n_{\max} and the bond dimension χ , and saturates at some point. An error on the order of 10^{-4} can be reached with a low-rank representation such as $\chi = 50$. For the DMFT calculation in the crossover region, we confirmed that the weak-coupling TCI solver can correctly repro-

duce the Green's functions obtained by QMC solvers. Using results obtained during the calculation of the Green's functions, we can also evaluate the doublon number and free energy of the lattice model with almost no extra effort. The latter quantity is difficult to calculate with QMC solvers. We also applied the TCI solver at lower temperature, where a first order Mott transition appears. We demonstrated the coexistence of two stable solutions and the associated hysteresis behavior in the doublon number, which are characteristics of the metal-to-Mott insulator transition. These findings establish the weak-coupling TCI solver as a reliable and efficient tool for the study of quantum impurity problems in the weak- and intermediate-interaction regimes.

The comparison of the TCI solver with other established methods highlights its strengths and limitations. One of the most notable advantages of the TCI solver over the CT-QMC methods is that it is free from the conventional sign problem. While the models analyzed in this paper do not exhibit a sign problem in QMC, the TCI solver will become more advantageous when applied to multi-orbital systems with off-diagonal hybridizations, multi-site clusters, systems with retarded spin interactions, spin-orbit coupled models or nonequilibrium impurity problems. In addition, the TCI solver facilitates the direct calculation of the free energy, which is a non-trivial problem for Monte Carlo techniques that lack information on the partition function.

On the other hand, there is room to improve the efficiency of the TCI solver. The TCI algorithm requires a large number of evaluations of the determinant in Eqs. (10) and (11) to construct a tensor-train representation. Since the computational cost of calculating determinants scales as $\mathcal{O}(n^3)$ with the size n of a matrix, the TCI algorithm becomes time-consuming for high-dimensional integrals. In CT-QMC, one evaluates the same type of determinants, but with a smaller cost of $\mathcal{O}(n^2)$ using the fast update algorithm [31]. In the TCI solver, such a technique is not available since the variable transformation changes the structure of the determinant. We will leave this issue as an interesting future problem.

Compared with wave-function-based solvers such as exact diagonalization (ED) [51–53] or the density matrix renormalization group (DMRG) [54–56], the TCI solver has the advantages of being free from finite-size effects and easily applicable to calculations at nonzero temperatures. Another method worth mentioning here is the influential functional (IF) method [57–61], a recently developed powerful solver for impurity problems. The IF method is similar to the TCI solver in that it decomposes a tensor into a product of small matrices. However, the objects being decomposed differ significantly: the TCI solver targets the integrand appearing in the perturbative expansion, while the IF method targets the discretized Feynman–Vernon IF, which encodes the time non-locality introduced by the bath. In the IF method, once the tensor-train representation of a given bath's IF is obtained, calculations for arbitrary interaction with that

bath can be performed easily. Nevertheless, constructing the tensor-train representation for the IF is computationally demanding. Moreover, since the bath is self-consistently determined and hence is updated for each iteration in the case of DMFT, the tensor-train decomposition of the IF must be performed multiple times, making the calculation more time-consuming. Thus, when dealing with impurity problems or DMFT for small (large) U , the weak-coupling (strong-coupling) TCI solver should be more efficient.

Finally, compared to the strong-coupling TCI solver [40], the weak-coupling TCI solver is expected to be better suited for addressing multi-site cluster impurity problems. In the strong-coupling expansion, the integrand includes a trace over the impurity Hilbert space. If the impurity Hamiltonian is diagonal in the occupation number basis, the segment formalism [31] enables a fast calculation of the trace. However, if it is not diagonal, one has to perform multiplications of matrices whose size grows exponentially with the number of orbitals or sites, which becomes the bottleneck of the calculation. On the other hand, in the weak-coupling expansion, in addition to the integral over the imaginary time as in Eqs. (4) and (5), we have discrete summations over the site indices in multi-site clusters or orbitals and interaction-type indices in multi-orbital systems. If the integrands with additional indices also exhibit a low-rank structure, similar to the single-site and single-orbital case, TCI can be used to efficiently evaluate the summations over these indices. In the weak-coupling TCI approach, the computational cost grows polynomially with the system size, the number of orbitals, and the number of interaction types. For multi-orbital models with general interactions, the number of interaction types grows as $\mathcal{O}(n_{\text{orb}}^4)$, where n_{orb} is the number of orbitals, and the tensor to be decomposed becomes large. Thus, treating such a multi-orbital model with general interactions will be challenging. It has been pointed out in Ref. [62] that the low-order skeleton diagrams in multi-orbital systems with retarded interactions exhibit a low-rank structure in the quantics representation [63, 64], which indicates the possibility of treating multi-orbital problems with the weak-coupling TCI. Whether higher-order diagrams also have a low-rank structure remains an open question, which should be investigated in future studies.

Overall, while the current implementation of the TCI solver leaves room for refinements, its unique features and capabilities make it a promising addition to the toolkit for studying strongly correlated electron systems. The potential of the weak-coupling TCI solver will be more clearly demonstrated in future applications to problems where the CT-QMC methods suffer from the sign problem.

ACKNOWLEDGEMENTS

S.M. and N.T. acknowledge support by JST FOREST (Grant No. JPMJFR2131) and JSPS KAKENHI (Grant No. JP24H00191). S.M. is also supported by the Forefront Physics and Mathematics Program to Drive Transformation (FoPM), a World-Leading Innovative Graduate Study (WINGS) Program, the University of Tokyo. H.S. is supported by JSPS KAKENHI (Grants Nos. 21H01041, 21H01003, 22KK0226, and 23H03817) as well as JST FOREST (Grant No. JPMJFR2232) and JST PRESTO (Grant No. JPMJPR2012). P.W. is supported by SNSF Grant No. 200021-196966. The calculation has been done with a code based on `TensorCrossInterpolation.jl` [39] and `SparseIR.jl` [47].

Appendix A: Change of variables

In this Appendix, we review the variable transformations which are used to change the integral domain from the simplex to the hypercube and to avoid the discontinuities of the integrand.

1. Transformation from $S_n^{a,b}$ to $S_n^{0,1}$

Let us consider changing the integral domain from $S_n^{a,b}$ into $S_n^{0,1}$ through a variable transformation. To this end, we use a map $f_n^{a,b} : S_n^{0,1} \rightarrow S_n^{a,b}$,

$$[f_n^{a,b}(\mathbf{y})]_i = a + (b - a)y_i, \quad (\text{A1})$$

where $\mathbf{y} = (y_1, \dots, y_n) \in S_n^{0,1}$. This map is clearly a bijection from $S_n^{0,1}$ to $S_n^{a,b}$ and its Jacobian is

$$J_{f_n^{a,b}}(\mathbf{y}) = \det \left(\frac{\partial f_n^{a,b}}{\partial \mathbf{y}} \right) = (b - a)^n. \quad (\text{A2})$$

If we relate the variables $\mathbf{x} \in S_n^{a,b}$ and $\mathbf{y} \in S_n^{0,1}$ by

$$\mathbf{x} = f_n^{a,b}(\mathbf{y}), \quad (\text{A3})$$

the integral over $S_n^{a,b}$ with respect to \mathbf{x} can be rewritten as an integral over $S_n^{0,1}$ with respect to \mathbf{y} :

$$\int_{S_n^{a,b}} d^n \mathbf{x} F(\mathbf{x}) = \int_{S_n^{0,1}} d^n \mathbf{y} F(f_n^{a,b}(\mathbf{y})) (b - a)^n. \quad (\text{A4})$$

2. Transformation from $S_n^{0,1}$ to $[0, 1]^n$

Let us consider changing the integral domain from the simplex $S_n^{0,1}$ to the unit hypercube $[0, 1]^n$. To this end,

we use a map $g_n : [0, 1]^n \rightarrow S_n^{0,1}$,

$$[g_n(\mathbf{z})]_i = 1 - \prod_{j=1}^{i-1} (1 - z_j), \quad (\text{A5})$$

where $\mathbf{z} = (z_1, \dots, z_n) \in [0, 1]^n$. This transformation is essentially the same as the one used in Ref. [40]. After some considerations, it becomes clear that this map is a bijection from $[0, 1]^n$ to $S_n^{0,1}$. Since the Jacobi matrix of this map is a lower triangular matrix, the Jacobian can be easily calculated as

$$\begin{aligned} J_{g_n}(\mathbf{z}) &= \det \left(\frac{\partial g_n}{\partial \mathbf{z}} \right) \\ &= (1 - z_1)^{n-1} (1 - z_2)^{n-2} \dots (1 - z_{n-1}). \end{aligned} \quad (\text{A6})$$

If we relate the variable $\mathbf{y} \in S_n^{0,1}$ with $\mathbf{z} \in [0, 1]^n$ by

$$\mathbf{y} = g_n(\mathbf{z}), \quad (\text{A7})$$

the integral over $S_n^{0,1}$ with respect to \mathbf{y} can be rewritten as an integral over $[0, 1]^n$ with respect to \mathbf{z} :

$$\int_{S_n^{0,1}} d^n \mathbf{y} F(\mathbf{y}) = \int_{[0,1]^n} d^n \mathbf{z} F(g_n(\mathbf{z})) J_{g_n}(\mathbf{z}). \quad (\text{A8})$$

3. Transformation from $S_n^{a,b}$ to $[0, 1]^n$

By combining the two maps, $f_n^{a,b}$ and g_n , we can construct a bijective map from $[0, 1]^n$ to $S_n^{a,b}$,

$$h_n^{a,b} = f_n^{a,b} \circ g_n. \quad (\text{A9})$$

The Jacobian of this map is given by

$$\begin{aligned} J_{h_n^{a,b}}(\mathbf{z}) &= J_{f_n^{a,b}}(g_n(\mathbf{z})) J_{g_n}(\mathbf{z}) \\ &= (b - a)^n (1 - z_1)^{n-1} \dots (1 - z_{n-1}). \end{aligned} \quad (\text{A10})$$

If we relate the variable $\mathbf{x} \in S_n^{a,b}$ with $\mathbf{z} \in [0, 1]^n$ by

$$\mathbf{x} = h_n^{a,b}(\mathbf{z}), \quad (\text{A11})$$

the integral over $S_n^{a,b}$ with respect to \mathbf{x} can be rewritten as an integral over $[0, 1]^n$ with respect to \mathbf{z} :

$$\int_{S_n^{a,b}} d^n \mathbf{x} F(\mathbf{x}) = \int_{[0,1]^n} d^n \mathbf{z} F(h_n^{a,b}(\mathbf{z})) J_{h_n^{a,b}}(\mathbf{z}). \quad (\text{A12})$$

-
- [1] J. Kondo, Resistance minimum in dilute magnetic alloys, *Prog. Theor. Phys.* **32**, 37 (1964).
- [2] A. M. Clogston, B. T. Matthias, M. Peter, H. J. Williams, E. Corenzwit, and R. C. Sherwood, Local Magnetic Moment Associated with an Iron Atom Dissolved in Various Transition Metal Alloys, *Phys. Rev.* **125**, 541 (1962).
- [3] M. P. Sarachik, E. Corenzwit, and L. D. Longinotti, Resistivity of Mo-Nb and Mo-Re Alloys Containing 1% Fe, *Phys. Rev.* **135**, A1041 (1964).
- [4] Y. Li, R. Deng, W. Lin, Y. Tian, H. Peng, J. Yi, B. Yao, and T. Wu, Electrostatic tuning of Kondo effect in a rare-earth-doped wide-band-gap oxide, *Phys. Rev. B* **87**, 155151 (2013).
- [5] D. Goldhaber-Gordon, H. Shtrikman, D. Mahalu, D. Abusch-Magder, U. Meirav, and M. A. Kastner, Kondo effect in a single-electron transistor, *Nature* **391**, 156 (1998).
- [6] S. M. Cronenwett, T. H. Oosterkamp, and L. P. Kouwenhoven, A Tunable Kondo Effect in Quantum Dots, *Science* **281**, 540 (1998).
- [7] I. V. Borzenets, J. Shim, J. Chen, A. Ludwig, A. Wieck, S. Tarucha, H.-S. Sim, and M. Yamamoto, Observation of the Kondo Screening Cloud of Micron Lengths, *Nature* **579**, 210 (2020).
- [8] A. V. Gorshkov, M. Hermele, V. Gurarie, C. Xu, P. S. Julienne, J. Ye, P. Zoller, E. Demler, M. D. Lukin, and A. Rey, Two-orbital $SU(N)$ magnetism with ultracold alkaline-earth atoms, *Nat. Phys.* **6**, 289 (2010).
- [9] L. Riegger, N. Darkwah Oppong, M. Höfer, D. R. Fernandes, I. Bloch, and S. Fölling, Localized Magnetic Moments with Tunable Spin Exchange in a Gas of Ultracold Fermions, *Phys. Rev. Lett.* **120**, 143601 (2018).
- [10] K. Ono, Y. Amano, T. Higomoto, Y. Saito, and Y. Takahashi, Observation of spin-exchange dynamics between itinerant and localized ^{176}Yb atoms, *Phys. Rev. A* **103**, L041303 (2021).
- [11] A. Georges and G. Kotliar, Hubbard model in infinite dimensions, *Phys. Rev. B* **45**, 6479 (1992).
- [12] A. Georges, G. Kotliar, W. Krauth, and M. J. Rozenberg, Dynamical mean-field theory of strongly correlated fermion systems and the limit of infinite dimensions, *Rev. Mod. Phys.* **68**, 13 (1996).
- [13] G. Kotliar, S. Y. Savrasov, K. Haule, V. S. Oudovenko, O. Parcollet, and C. A. Marianetti, Electronic structure calculations with dynamical mean-field theory, *Rev. Mod. Phys.* **78**, 865 (2006).
- [14] H. Aoki, N. Tsuji, M. Eckstein, M. Kollar, T. Oka, and P. Werner, Nonequilibrium dynamical mean-field theory and its applications, *Rev. Mod. Phys.* **86**, 779 (2014).
- [15] Q. Sun and G. K.-L. Chan, Quantum Embedding Theories, *Acc. Chem. Res.* **49**, 2705 (2016).
- [16] M. Jarrell, Hubbard model in infinite dimensions: A quantum Monte Carlo study, *Phys. Rev. Lett.* **69**, 168 (1992).
- [17] X. Y. Zhang, M. J. Rozenberg, and G. Kotliar, Mott transition in the $d = \infty$ Hubbard model at zero temperature, *Phys. Rev. Lett.* **70**, 1666 (1993).
- [18] R. Bulla, Zero Temperature Metal-Insulator Transition in the Infinite-Dimensional Hubbard Model, *Phys. Rev. Lett.* **83**, 136 (1999).
- [19] N. Blümer, Metal-Insulator Transition and Optical Conductivity in High Dimensions (Shaker Verlag, Aachen, 2003).
- [20] A. I. Lichtenstein and M. I. Katsnelson, Antiferromagnetism and d -wave superconductivity in cuprates: A cluster dynamical mean-field theory, *Phys. Rev. B* **62**, R9283 (2000).
- [21] T. Maier, M. Jarrell, T. Pruschke, and M. H. Hettler, Quantum cluster theories, *Rev. Mod. Phys.* **77**, 1027 (2005).
- [22] K. Haule and G. Kotliar, Strongly correlated superconductivity: A plaquette dynamical mean-field theory study, *Phys. Rev. B* **76**, 104509 (2007).
- [23] M. Kitatani, N. Tsuji, and H. Aoki, FLEX+DMFT approach to the d -wave superconducting phase diagram of the two-dimensional Hubbard model, *Phys. Rev. B* **92**, 085104 (2015).
- [24] D. Tanasković, V. Dobrosavljević, E. Abrahams and G. Kotliar, Disorder Screening in Strongly Correlated Systems, *Phys. Rev. Lett.* **91**, 066603 (2003).
- [25] K. Byczuk, W. Hofstetter, and D. Vollhardt, Mott-Hubbard Transition versus Anderson Localization in Correlated Electron Systems with Disorder, *Phys. Rev. Lett.* **94**, 056404 (2005).
- [26] K. Byczuk, W. Hofstetter, and D. Vollhardt, Anderson localization vs. Mott-Hubbard metal-insulator transition in disordered, interacting lattice fermion systems, *Int. J. Mod. Phys. B* **24**, 1727 (2010).
- [27] A. N. Rubtsov, V. V. Savkin, and A. I. Lichtenstein, Continuous-time quantum Monte Carlo method for fermions, *Phys. Rev. B* **72**, 035122 (2005).
- [28] P. Werner, A. Comanac, L. de' Medici, M. Troyer, and A. J. Millis, Continuous-time solver for quantum impurity models, *Phys. Rev. Lett.* **97**, 076405 (2006).
- [29] E. Gull, P. Werner, A. Millis, and M. Troyer, Performance analysis of continuous-time solvers for quantum impurity models, *Phys. Rev. B* **76**, 235123 (2007).
- [30] E. Gull, P. Werner, O. Parcollet, and M. Troyer, Continuous-time auxiliary-field Monte Carlo for quantum impurity models, *Europhys. Lett.* **82**, 57003 (2008).
- [31] E. Gull, A. J. Millis, A. I. Lichtenstein, A. N. Rubtsov, M. Troyer, and P. Werner, Continuous-time Monte Carlo methods for quantum impurity models, *Rev. Mod. Phys.* **83**, 349 (2011).
- [32] M. Maćek, P. T. Dumitrescu, C. Bertrand, B. Triggs, O. Parcollet, and X. Waintal, Quantum Quasi-Monte Carlo Technique for Many-Body Perturbative Expansions, *Phys. Rev. Lett.* **125**, 047702 (2020).
- [33] C. Bertrand, D. Bauernfeind, P. T. Dumitrescu, M. Maćek, X. Waintal, and O. Parcollet, Quantum quasi Monte Carlo algorithm for out-of-equilibrium Green functions at long times, *Phys. Rev. B* **103**, 155104 (2021).
- [34] I. Oseledets and E. Tyrtyshnikov, TT-cross approximation for multidimensional arrays, *Linear Algebra and its Applications* **432**(1), 70 (2010).
- [35] I. V. Oseledets, Tensor-train decomposition, *SIAM J. Sci. Comput.* **33**(5), 2295 (2011).
- [36] D. V. Savostyanov, Quasioptimality of maximum-volume cross interpolation of tensors, *Linear Algebra and its Applications* **458**, 217 (2014).

- [37] S. Dolgov and D. Savostyanov, Parallel cross interpolation for high-precision calculation of high-dimensional integrals, *Computer Physics Communications* **246**, 106869 (2020).
- [38] Y. Núñez-Fernández, M. Jeannin, P. T. Dumitrescu, T. Kloss, J. Kaye, O. Parcollet, and X. Waintal, Learning Feynman Diagrams with Tensor Trains, *Phys. Rev. X* **12**, 041018 (2022).
- [39] Y. Núñez-Fernández, M. K. Ritter, M. Jeannin, Jheng-Wei Li, T. Kloss, T. Louvet, S. Terasaki, O. Parcollet, Jan von Delft, H. Shinaoka, and X. Waintal, Learning tensor networks with tensor cross interpolation: new algorithms and libraries, arXiv:2407.02454 (2024).
- [40] A. Erpenbeck, W.-T. Lin, T. Blommel, L. Zhang, S. Isakov, L. Bernheimer, Y. Núñez-Fernández, G. Cohen, O. Parcollet, X. Waintal, and E. Gull, Tensor train continuous time solver for quantum impurity models, *Phys. Rev. B* **107**, 245135 (2023).
- [41] M. Eckstein, Solving impurity models in the non-equilibrium steady state with tensor trains, arXiv:2410.19707 (2024).
- [42] A. J. Kim and P. Werner, Strong coupling impurity solver based on quantics tensor cross interpolation, arXiv:2411.19026 (2024).
- [43] W. Metzner and D. Vollhardt, Correlated Lattice Fermions in $d = \infty$ Dimensions, *Phys. Rev. Lett.* **62**, 324 (1989).
- [44] H. Shinaoka, J. Otsuki, M. Ohzeki, and K. Yoshimi, Compressing Green's function using intermediate representation between imaginary-time and real-frequency domains, *Phys. Rev. B* **96**, 035147 (2017).
- [45] J. Li, M. Wallerberger, N. Chikano, C.-N. Yeh, E. Gull, and H. Shinaoka, Sparse sampling approach to efficient *ab initio* calculations at finite temperature, *Phys. Rev. B* **101**, 035144 (2020).
- [46] H. Shinaoka, N. Chikano, E. Gull, J. Li, T. Nomoto, J. Otsuki, M. Wallerberger, T. Wang, and K. Yoshimi, Efficient *ab initio* many-body calculations based on sparse modeling of matsubara green's function, *SciPost Phys. Lect. Notes* **63**, 1 (2022).
- [47] M. Wallerberger, S. Badr, S. Hoshino, F. Kakizawa, T. Koretsune, Y. Nagai, K. Nogaki, T. Nomoto, H. Mori, J. Otsuki, S. Ozaki, R. Sakurai, C. Vogel, N. Witt, K. Yoshimi and H. Shinaoka, sparse-ir: optimal compression and sparse sampling of many-body propagators, *SoftwareX* **16**, 100839 (2022).
- [48] J. K. Freericks and V. Zlatić, Exact dynamical mean-field theory of the Falicov-Kimball model, *Rev. Mod. Phys.* **75**, 1333 (2003).
- [49] G. Kotliar, E. Lange, and M.J. Rozenberg, Landau Theory of the Finite Temperature Mott Transition, *Phys. Rev. Lett.* **84**, 5180 (2000).
- [50] G. Kotliar, Sahana Murthy, and M. J. Rozenberg, Compressibility Divergence and the Finite Temperature Mott Transition, *Phys. Rev. Lett.* **89**, 046401 (2002).
- [51] M. Caffarel and W. Krauth, Exact diagonalization approach to correlated fermions in infinite dimensions: Mott transition and superconductivity, *Phys. Rev. Lett.* **72**, 1545 (1994).
- [52] M. Capone, L. de Medici, and A. Georges, Solving the Dynamical Mean-Field Theory at Very Low Temperatures Using the Lanczos Exact Diagonalization, *Phys. Rev. B* **76**, 245116 (2007).
- [53] A. Liebsch and H. Ishida, Temperature and bath size in exact diagonalization dynamical mean field theory, *J. Phys.: Condens. Matter* **24**, 053201 (2012).
- [54] F. A. Wolf, I. P. McCulloch, O. Parcollet, and U. Schollwöck, Chebyshev matrix product state impurity solver for dynamical mean-field theory, *Phys. Rev. B* **90**, 115124 (2014).
- [55] M. Ganahl, P. Thunström, F. Verstraete, K. Held, and H. G. Evertz, Chebyshev expansion for impurity models using matrix product states, *Phys. Rev. B* **90**, 045144 (2014).
- [56] F. A. Wolf, A. Go, I. P. McCulloch, A. J. Millis, and U. Schollwöck, Imaginary-Time Matrix Product State Impurity Solver for Dynamical Mean-Field Theory, *Phys. Rev. X* **5**, 041032 (2015).
- [57] J. Thoenniss, A. Leroose, and D. A. Abanin, Nonequilibrium quantum impurity problems via matrix-product states in the temporal domain, *Phys. Rev. B* **107**, 195101 (2023).
- [58] J. Thoenniss, M. Sonner, A. Leroose, and D. A. Abanin, Efficient method for quantum impurity problems out of equilibrium, *Phys. Rev. B* **107**, L201115 (2023).
- [59] R. Chen, X. Xu and C. Guo, Grassmann time-evolving matrix product operators for quantum impurity models, *Phys. Rev. B* **109**, 045140 (2024).
- [60] R. Chen and C. Guo, Solving equilibrium quantum impurity problems on the L-shaped Kadanoff-Baym contour, *Phys. Rev. B* **110**, 165114 (2024).
- [61] Z. Sun, R. Chen, Z. Li, and C. Guo, Infinite Grassmann time-evolving matrix product operators for non-equilibrium quantum impurity problems, arXiv:2412.04702 (2024).
- [62] H. Ishida, N. Okada, S. Hoshino and H. Shinaoka, Low-rank quantics tensor train representations of Feynman diagrams for multiorbital electron-phonon models, arXiv:2405.06440 (2024).
- [63] H. Shinaoka, M. Wallerberger, Y. Murakami, K. Nogaki, R. Sakurai, P. Werner, and A. Kauch, Multiscale Space-Time Ansatz for Correlation Functions of Quantum Systems Based on Quantics Tensor Trains, *Phys. Rev. X* **13**, 021015 (2023).
- [64] M. K. Ritter, Y. Núñez Fernández, M. Wallerberger, J. von Delft, H. Shinaoka, and X. Waintal, Quantics Tensor Cross Interpolation for High-Resolution Parsimonious Representations of Multivariate Functions, *Phys. Rev. Lett.* **132**, 056501 (2024).